I. COLLIDER STORAGE RING

A. Introduction

After acceleration, both μ^+ and μ^- bunches are injected into a separate storage ring. The highest possible average bending field is desirable, to maximize the number of revolutions before decay, and thus maximize the luminosity. Collisions would occur in one, or perhaps two, low-β^* interaction areas. Parameters of the rings were given earlier in Tb. **??**.

B. Lattice Design

In order to maintain the required short bunches without excessive rf, the ring must be approximately, or fully, isochronous.

The required β functions at the intersection point are small for a 3 TeV collider, we require $\beta^* = 3\,\mathrm{mm}$, and the quadrupoles needed to generate them are large (20-30 cm diameter). At 100 GeV CoM, the β's at the IP are not that small, and the quadrupoles are more conventional, but in both cases it has been found that local chromatic correction is essential [1–4].

The rings are racetracks, with two circular arcs separated by an experimental insertion, on one side, and a utility insertion for injection, extraction, and beam scraping, on the other. The experimental insertion includes the interaction region (IR) followed by a local chromatic correction (CCS) and a matching section. The chromatic correction section is optimized to correct the ring's linear chromaticity, which is almost completely generated by the IR.

The bending magnets would be superconducting. The magnets must be shielded from the electrons emitted by decay of the beam. Fields of 8 T have been assumed in the 100 GeV lattices described below, but higher field dipoles would reduce the ring diameters a nd increase luminosity. Studies of higher field dipoles have been started.

The rf requirements depend on the lattice momentum compaction and bunch parameters. For the very low momentum spread Higgs collider parameters, synchrotron motion does not occur and rf is used solely to correct impedance generated momentum spread in the bunch. For the higher momentum spread cases, there are two options. If the momentum compaction can be corrected to high order then synchrotron motion can still be eliminated and the rf is again only used for energy spread correction. Alternatively, if some momentum compaction is retained, then significant rf is needed to maintain the specified short bunches. In either case rf quadrupoles will be required to generate BNS [5] damping of the transverse head-tail instability (beam breakup).

C. Lattices

Preliminary lattices have been designed for both 4 TeV and 0.5 TeV machines [6], and several designs now exist for the 100 GeV case. For the 100 GeV CoM collider, two operating cases are being considered a high-luminosity case with broad momentum acceptance to accommodate a beam with a $\delta p/p$ of $\pm 0.12\%$ (rms) and one with a much narrower momentum acceptance and lower luminosity for beam with $\delta p/p$ of $\pm 0.003\%$ (rms). For the broad momentum acceptance case, the β^* must be 4 cm and for narrow momentum acceptance, 13 cm. In either case, the bunch length must be held comparable to the value of β^*. It is assumed that a single lattice can be designed that can operate in either mode by adjusting settings.

We describe below two examples of 100 GeV designs. They were generated by two different semi-independent, but converging, studies. The primary difference between the two is in the flexible momentum compaction arc modules.

1. 100 GeV example (a)

This design, shown in Fig. 1, has a total circumference of about 350 m with arc modules accounting for only about a quarter of the ring circumference.

The low-beta function values at the IP are mainly produced by three strong superconducting quadrupoles in the Final Focus Telescope (FFT) with pole-tip fields of 8 T. The full interaction region is symmetric with reflection about the intersection point (IP). Because of significant, large-angle backgrounds from muon decay, a background-sweep dipole must be included in the final focus telescope and placed near the IP to protect the detector [7]. It was found that 2.5 m of an 8 T field was required to attain sufficient background suppression. The first quadrupole is located 5 m away from the interaction point, the beta reaches a maximum of 1.5 km in the final focus telescope when the

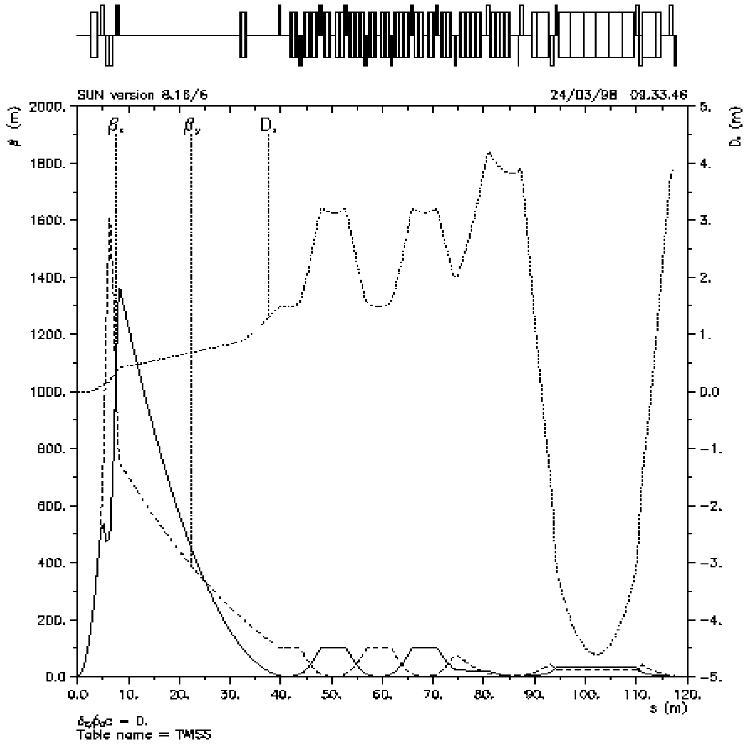

FIG. 1. Example (a) of a 50-GeV Muon Collider: Half of the IR, local chromatic correction, and one of three arc modules.

beta functions are equalized in both planes. For this value of beta, quadrupole apertures must be at least 15 cm in radius to accommodate $5\,\sigma$ of an $90\ \pi$ mm-mr, 50-GeV muon beam (normalized rms emittance) plus a 2 to 3 cm thick tungsten liner [8]. The natural chromaticity of this interaction region is about -60.

Local chromatic correction of all muon collider interaction regions is required to achieve broad momentum acceptance. The basic approach developed by Brown [2] and others [9], is used. Two pairs of sextupoles, one pair in each plane, are separated by a phase advance of π, all in high dispersion, with each being $(2n+1)\pi/2$ from the IP. The geometric aberrations of each sextupole is canceled by its companion while the chromaticity corrections add.

In our case, this chromatic correction section design (Fig. 2) was optimized to be as short possible. The $\beta_{\rm max}$ of only 100 m and a $\beta_{\rm min}$ less than 1 m ($\beta_{\rm min}$ = 0.7 m), giving a $\beta_{\rm ratio}$ between planes of about 150 without compromising aperture by a large amplitude dependent tuneshift.

The sextupoles are centered about the opposite-plane minimum ($\beta_{min} < 1$), which provides a chromatic correction with minimal cross correlation between planes. A further advantage to locating the opposite-plane minimum at the center of the sextupole is that this point is $\pi/2$ away from, or, "out of phase" with the chromatic effects from the final-focus quadrupoles; i.e. the plane not being chromatically corrected is treated like the IP in terms of phase to eliminate a second order chromatic aberration arising from the sextupole.

The large beta ratio combined with the opposite-plane phasing allowed sextupoles for opposite planes to be interleaved without significantly impacting lattice nonlinearity. In point of fact, interleaving improved lattice performance over a non-interleaved correction scheme, primarily due to a shortening of the chromatic correction section, which is accompanied by a lowering of its contribution to overall chromaticity [10]. Shallower minima and less variations in beta were also applied to soften chromatic aberrations, but at the expense of an exact π phase separation between sextupole partners. The retention of an exact π phase difference between sextupoles was found to be less important to the dynamic aperture than elimination of minima with $\beta_{\rm min} < 0.5$ m.

The momentum compaction of the IR, chromatic correction section, and matching sections is about 0.04. Since the length of this part is 173 m, the 93 m arc length must have a negative momentum compaction of about -0.09 in order to offset the positive portion of the ring.

The arc module Fig. 3 has the small beta functions characteristic of FODO cells, yet a large, almost separate, variability in the momentum compaction of the module which is a characteristics associated with the flexible momentum compaction module [11]. The smallish beta functions are achieved through the use of a doublet focusing structure which produces a low beta simultaneously in both planes. At the dual minima, a strong focusing quadrupole is

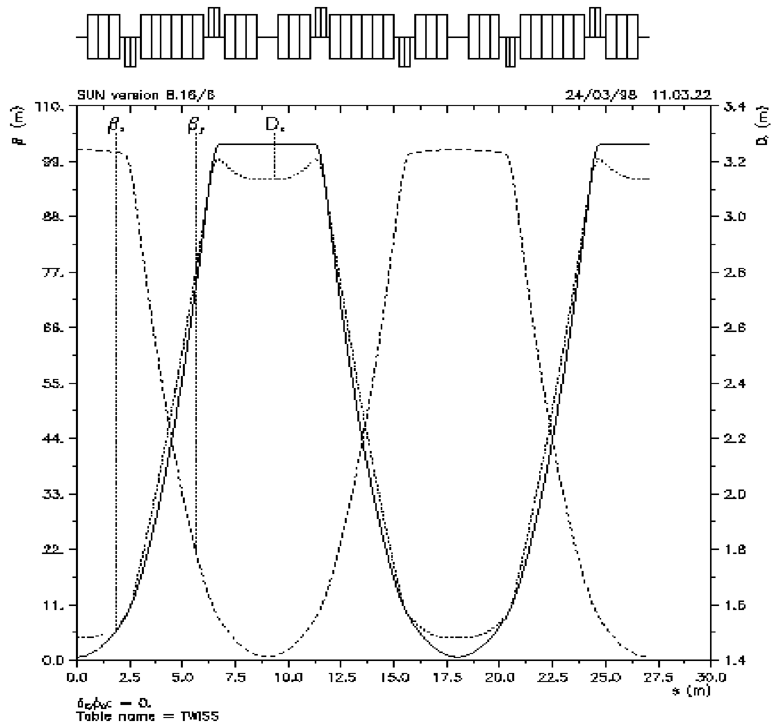

FIG. 2. The 50-GeV Muon Collider: The Chromatic Correction Module.

placed to control the derivative of dispersion with little impact on the beta functions. Negative values of momentum compaction as low as $\alpha = -0.13$ been achieved, and $\gamma_t = 2$ i, been achieved with modest values of the beta function.

This arc module was able to generate the needed negative momentum compaction with beta functions of 40 m or less. The peak dispersion is somewhat high, 4.6 m and need to be reduced.

A very preliminary dynamic aperture [12] without optimization of the lattice nor inclusion of errors and end effects is given in Fig. 4.

For the very low momentum spread operation, a larger acceptance is required. This should be possible by turning the sextupoles off. The result of doing this is also shown in the figure (dashed line). The momentum acceptance is lost, as expected, but the gain in transverse acceptance, though real, is disappointing. More work is needed.

2. 100 GeV example (b)

The second lattice is shown in Fig. 5 starting from the IP.

The 1.5 m background clearing dipole is 2.5 m away from the IP and is followed by the triplet quadrupoles with the focusing quadrupole in the center. The interaction region (IR) stops at about 24 m from the IP and the local correction section begins. The Twiss properties at the centers of the 4 correction sextupoles are listed in Tb. I.

TABLE I. Twiss properties of the interaction region correction sextupoles.

	Distance (m)	Phase Advances ν_x	ν_y	Betatron Functions (m) β_x	β_y	Dispersion (m)
SX2	33.5061	0.48826	0.74953	1.00000	100.00012	2.37647
SX2	62.3942	0.98707	1.24953	1.00000	100.00009	2.37651
SX1	49.3327	0.74892	0.87703	100.00023	1.00000	2.66039
SX1	74.6074	1.24892	1.47987	99.99967	0.99992	2.65817

We denote with SX1 the two horizontal correction sextupoles. They are placed at positions with the same betatron functions and dispersion function, and are separated horizontally and vertically by phase advances π so that their nonlinear effect will be confined in the region between the two sextupoles. Their horizontal phase advances are also

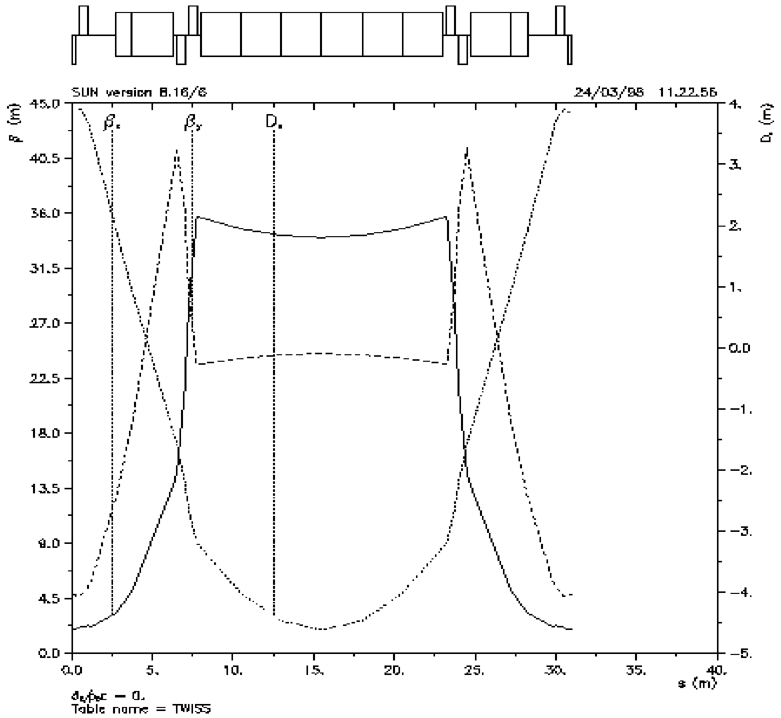

FIG. 3. The 50-GeV Muon Collider: A New Flexible Momentum Compaction Arc Module.

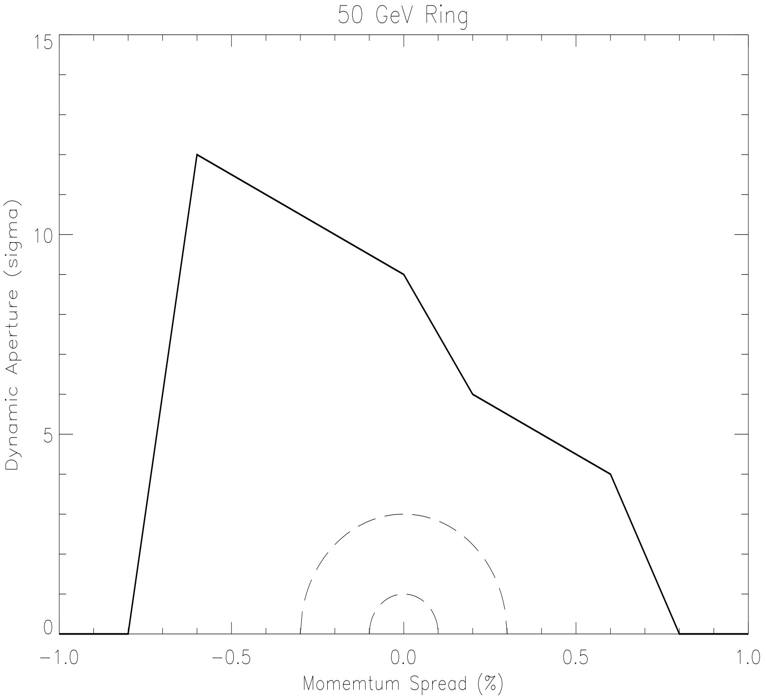

FIG. 4. The 50-GeV Muon Collider: A preliminary dynamic aperture.

integer numbers of π from the triplet focusing F-quadrupole so that the chromaticity compensation for that quadrupole will be most efficient [9]. The SX2's are the two vertical correction sextupoles and are placed similarly at designated

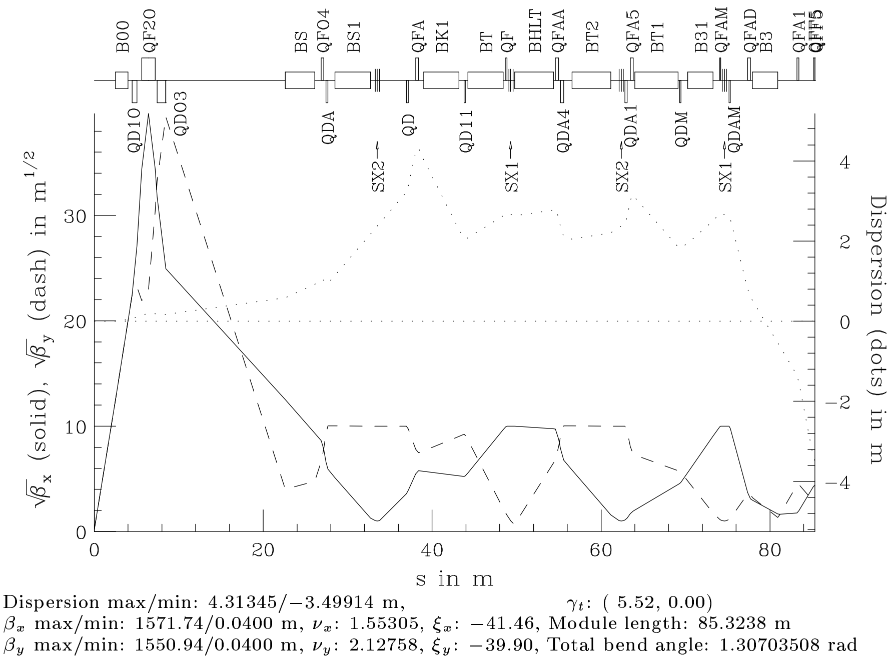

FIG. 5. Example (b) structure of the interaction region including local chromaticity corrections.

locations. Notice that the correction section on each side of the IP spans a distance of roughly 61.3 m.

Flexible momentum-compaction (FMC) modules [13] are used in the arc. The momentum compaction of the arc has to be made negative in order to cancel the positive momentum compaction of the IR, so that the whole ring becomes quasi-isochronous. This is accomplished in three ways: removing the central dipole of the standard FMC module, by increasing the length of the first and last dipoles, and by increasing the negative dispersion at entrance. Two of such modules is required for half of the collider ring, one of which is shown in Fig. 6.

To close the ring geometrically, there will be a ~ 72.0 m straight section between the two sets of FMC modules. The total length of the collider ring is now 354.3 m. Note that the interaction region and local correction sections take up 48.2% of the whole ring. The momentum-compaction factor of the whole ring is now $\alpha_0 = -2.77 \times 10^{-4}$. If the bucket height is taken as $k = 8$ times the rms momentum spread of the bunch, an rf voltage of $V_{\rm rf} \approx 770(\frac{\delta p}{p})^2$ kV will be required. Since α_0 is negative already, its absolute value can be further lowered easily. However, we must make sure that the contributions from the higher-order momentum compaction are small also. This will be studied. Note that there are not yet families of sextupoles to correct for the higher order chromaticities in this ring with only 4 FMC modules.

The dynamical aperture of the lattice is computed by tracking particles with the code COSY [14]. We track 16 particles with the same momentum offset and x' and y' placed uniformly on a very small circle. If all particles survive, then the radius is increased and the tracking repeated. The largest radius that provide survival of the 16 particles in 1000 turns is defined here as the dynamical aperture at this momentum offset and is plotted in solid in Fig. 7(a) in units of the rms radius of the beam at the IP. (At the 4 cm low-beta IP, the beam has an rms radius of 82 μm). As a reference, the 7-sigma aperture spanning ± 5 sigmas of momentum offset is also displayed as a semi-ellipse in dots. To maximize the aperture, first, the tunes must be chosen to avoid parametric resonances. The on-momentum amplitude dependent horizontal and vertical tunes are

$$\begin{aligned} \nu_x &= 8.126337 - \ 100\epsilon_x - 4140\epsilon_y \ , \\ \nu_y &= 6.239988 - 4140\epsilon_x - 54.6\epsilon_y \ , \end{aligned}$$

where ϵ_x and ϵ_y are the horizontal and vertical unnormalized emittance in πm. With the designed rms $\epsilon_x = \epsilon_y = 0.169\ \pi$m, the variations appear to be small. Second, the chromaticity variations with momentum must be as small as possible. This is shown in Fig. 7(b). For momentum spread varying from -1 to 0.9%, ν_x varies from 8.16698 to 8.07459, and ν_y from 6.28305 to 6.22369 for the center of the beam.

During aperture tracking we notice particle loss occurs mostly in the horizontal direction. We are convinced that the small aperture is a result of the large dispersion swing in the lattice from $+4.5$ to -3.5 m. For example, -4.5 m dispersion and 0.6% momentum offset translates into a 2.7 cm off-axis motion. The nonlinearity of the lattice will

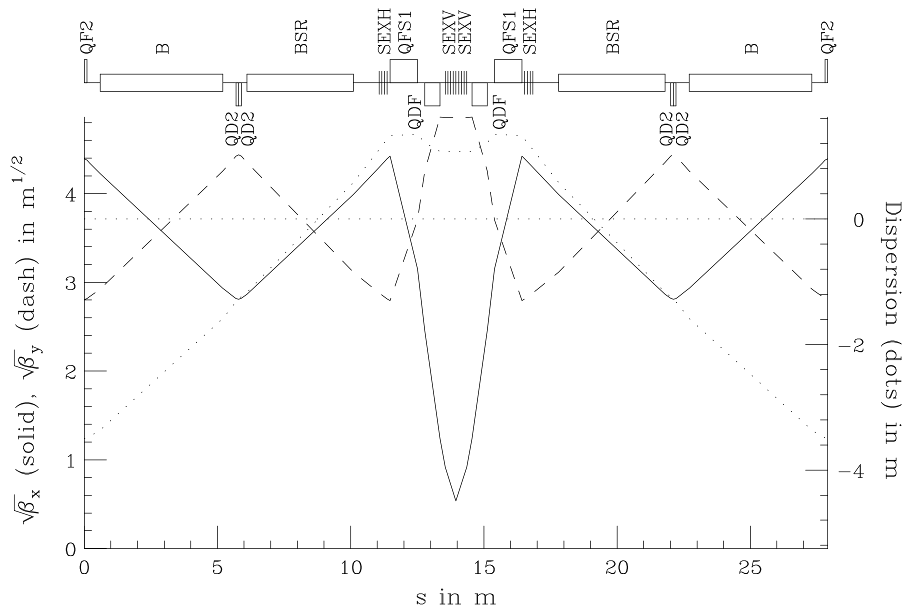

Dispersion max/min: 1.35084/−3.50000 m, γ_t: (0.00, 4.43)
β_x max/min: 19.57/0.28915 m, ν_x: 0.75506, ξ_x: −1.77, Module length: 27.9062m
β_y max/min: 23.63/7.80157 m, ν_y: 0.36290, ξ_y: −0.92, Total bend angle: 0.9170180 rad

FIG. 6. Lattice structure of the flexible momentum-compaction module.

therefore diminish the dynamical aperture. A resonant strength study actually reveals that this lattice is unusually nonlinear. Recently, we make a modification of the flexible momentum compaction arc modules which have a smaller dispersion swing from −2.6 to +2.0 m only. The interaction region was not changed except for the matching to the arc modules. The aperture has was tracked with TEAPOT [15] in the same way as COSY and is plotted as dashes in Fig. 7(a). We see that the momentum aperture is wider, but the aperture near on-momentum is one sigma less than the lattice presented here. Nevertheless, this may not be so much less, because all trackings have been performed in steps of one sigma only.

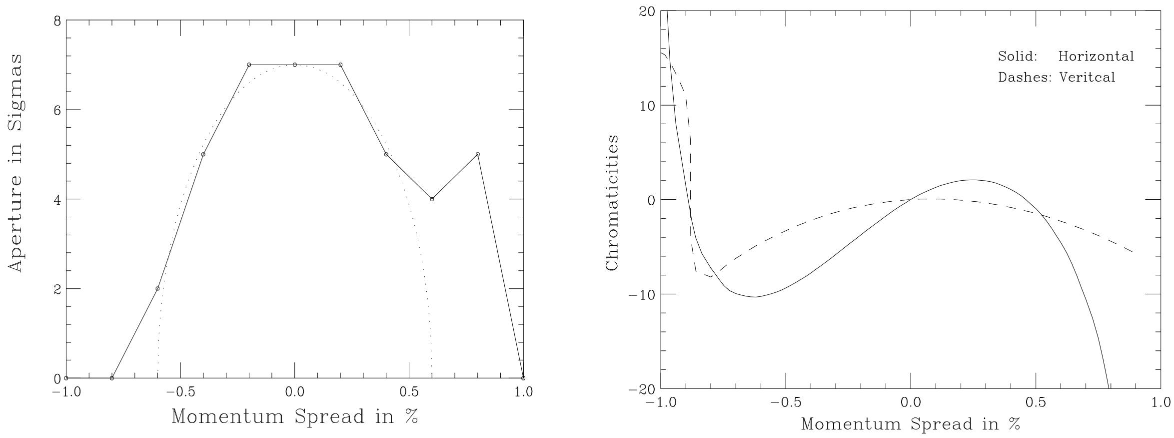

(a) (b)

FIG. 7. (a) Dynamical aperture of the lattice *vs.* momentum offset. (b) Chromaticities *vs.* momentum offset.

D. Scraping

It has been shown [16] that detector backgrounds originating from beam halo can exceed those from decays in the vicinity of the interaction point (IP). Only with a dedicated beam cleaning system far enough from the IP can one mitigate this problem [8]. Muons injected with large momentum errors or betatron oscillations will be lost within the first few turns. After that, with active scraping, the beam halo generated through beam-gas scattering, resonances and beam-beam interactions at the IP reaches equilibrium and beam losses remain constant throughout the rest of the cycle.

Two beam cleaning schemes have been designed [8]. One for muon colliders at high energies, and one for those at low energies.

The studies [8] showed that no absorber, ordinary or magnetized, will suffice for beam cleaning at 2 TeV; in fact the disturbed muons are often lost in the IR, but a simple metal collimator was found to be satisfactory at 100 GeV.

1. Scraping for High Energy Collider

At high energies, a 3-m long electrostatic deflector (Fig. 8) separates muons with amplitudes larger than 3σ and deflects them into a 3-m long Lambertson magnet, which extracts these downwards through a deflection of 17 mrad. A vertical septum magnet is used in the vertical scraping section instead of the Lambertson to keep the direction of extracted beam down. The shaving process lasts for the first few turns. To achieve practical distances and design apertures for the separator/Lambertson combinations, β-functions must reach a kilometer in the 2-TeV case, but only 100 m at 50 GeV. The complete system consists of a vertical scraping section and two horizontal ones for positive and negative momentum scraping (the design is symmetric about the center, so scraping is identical for both μ^+ and μ^-). The system provides a scraping efficiency of a factor of 1000.

2. Scraping for Low Energy Collider

At 50 GeV, collimating muon halos with a 5-m long steel absorber (Fig. 9) in a simple compact utility section does an excellent job. Muons loose a significant fraction of their energy in such an absorber (8% on average) and have broad angular and spatial distributions. Almost all of these muons are then lost in the first 50-100 m downstream of the absorber with only 0.07% of the scraped muons reaching the low-β quadrupoles in the IR, i. e. a scraping efficiency is 1500 in this case, which is significantly better than with in an earlier septum scraping system [8] similar to that developed for the high energy collider.

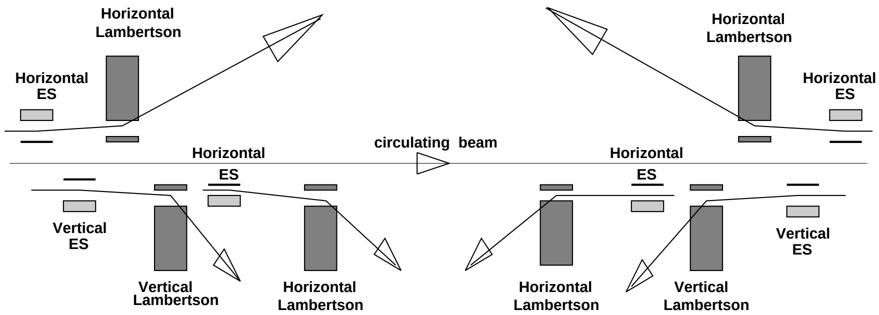

FIG. 8. Schematic view of a $\mu^+\mu^-$collider beam halo extraction.

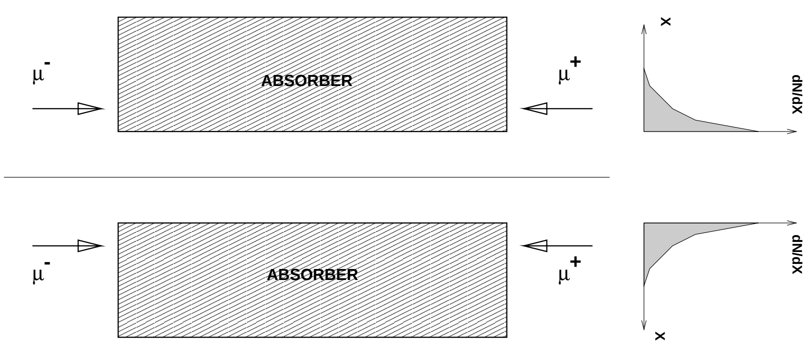

FIG. 9. Scraping muon beam halo with a 5-m steel absorber.

E. Beam-Beam Tune Shift

Several studies have considered beam emittance growth due to beam-beam tune shift and none observed significant luminosity loss. For instance, a study [17], using the high energy collider parameters (Tb.??), in which particles were tracked assuming Gaussian beam field distributions, and no muon decay, showed a luminosity loss of only 4 %. With muon decay included, the loss contribution from beam-beam effects is even less. Another study [18] using a particle in cell approach with no assumptions about field symmetry obtained a similar result. Collisions between beams displaced by 10 % of their radius also gave little loss. But all these studies assumed an ideal lattice, and none considered whether a very small fraction of the beam may be lost, giving probably unacceptable background. More work is in progress.

F. Impedance/Wake Field Considerations

A study [19] has examined the resistive wall impedance longitudinal instabilities in rings at several energies. At the higher energies and larger momentum spreads, solutions were found with small but finite momentum compaction, and moderate rf. For the special case of the Higgs Factory, with its very low momentum spread, a solution was found with no synchrotron motion, but rf provided to correct the first order impedance generated momentum spread. The remaining off-momentum tails, that would not affect the luminosity, but which might generate background, could be removed by a higher harmonic rf correction. Solutions to the higher energy and larger momentum spread cases without synchrotron motion are also being considered.

Given the very slow, or nonexistent synchrotron oscillations, the transverse beam breakup instability is significant. This instability can be stabilized using rf quadrupole [5] induced BNS damping. For instance, in the 3 TeV case, to stabilize the resistive wall instability, the required tune shift with position in the bunch, calculated [20] using the two particle model approximation, for a 1 cm radius aluminum pipe, is only 1.58×10^{-4}. However, this application of the BNS damping to a quasi-isochronous ring, and other head-tail instabilities due to the chromaticities ξ and η_1, needs more careful study.

G. Bending Magnet Design

The dipole fields assumed in the 100 GeV collider lattices described above was 8 T. This field can be obtained using 1.8n is the need for a tungsten shield between the beam and coils to shield the latter from beam decay heating.

The μ's decay within the rings ($\mu^- \to e^- \overline{\nu_e} \nu_\mu$), producing electrons whose mean energy is approximately 0.35 that of the muons. With no shielding, the average power deposited per unit length would be about 2 kW/m in the 4 TeV machine, and 300 W/m in the 100 GeV Higgs factory. Figure 10 shows the power penetrating tungsten shields of different thickness [21,7,8,22]. One sees that 3 cm in the low energy case, or 6 cm at high energy would reduce the power to below 10 W/m, which can reasonably be taken by superconducting magnets.

Figure11 shows the cross section of a baseline magnet suitable for the 100 GeV collider.

The quadrupoles could use warm iron poles placed as close to the beam as practical. The coils could then be either superconducting or warm, placed at a greater distance from the beam and shielded from it by the poles.

The collider ring could be made smaller, and the luminosity increased, if higher field dipoles were used. In the low energy case, the gain would not be great since less than half the circumference is devoted to arc. For this reason, and to avoid yet another technical challenge, higher field magnets are not part of the baseline design of a 100 GeV collider. But they would give a significant luminosity improvement for the higher energy colliders, and would be desirable there. There have been several studies of possible designs, three of which (two that are promising and one that appears not to work) are included below.

1. Alternative Racetrack Nb_3Sn dipole

A higher field magnet based on Nb_3Sn conductor and racetrack coils is presently being designed.The Nb_3Sn conductor allows higher fields and provides a high temperature margin over the operating temperature, but being brittle and sensitive to bending or other stress, presents a number of engineering challenges.

In this design, the stress levels in the conductor are reduced by the use of a rectangular coil block geometry and end support problems are reduced by keeping the coils flat. In the more conventional "cos theta" designs, the conductor

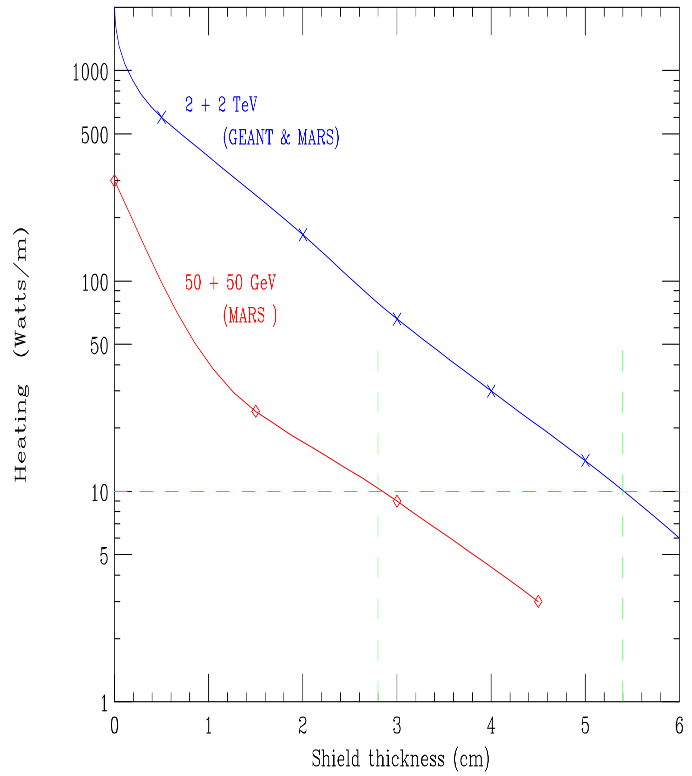

FIG. 10. Power penetrating tungsten shields vs. their thickness for a) 4 TeV, and b) 100 GeV, collider.

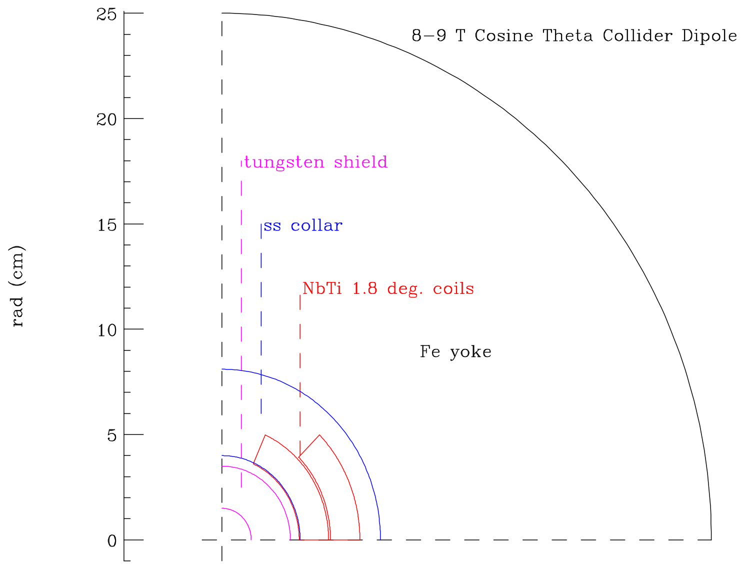

FIG. 11. Cross Section of a Baseline Dipole Magnet Suitable for the 100 GeV Collider.

is distributed around a cylinder and the forces add up towards the mid-plane. And the ends, as the arc over the cylinder, are relatively hard to support.

The geometry of the cross section is shown in Fig.12. It uses all 2-D flat racetrack coils. Each quadrant of the magnet aperture has two blocks of conductors. The block at the pole in the first quadrant has a return block in the second quadrant, similar to that in the conventional design. The height of this block is such that it completely clears the bore. In a conventional design, the second block, the midplane block, would also have a return block in the second quadrant. That would, however, require the conductor block to be lifted up in the ends to clear the bore and thus would loose the simple 2-D geometry. In the proposed design, the return block retains the 2-D coil geometry as it is returned on the same side (see Fig.12) and naturally clears the bore. Since the return block does not contribute to the field, this design uses 50 % more conductors. This, however, is a small penalty to pay for a few magnets where the performance and not the cost is a major issue. The field lines are also shown in Fig.12.

Preliminary design parameters for two cases are given here. The first case is one when the performance of the cable used in both cases is the same that is in LBL D20 magnet, which created a central field of 13.5 T. The second case is the one when the cable is graded and two types of cables are used, and it is assumed that a reported improvements in cable performance is realized. It is expected to produce a central field of 14.7 T when operated at 4.2 ^oK.

Case 1: Same conductor as in LBL 13.5 T D20 magnet without grading

Central field at quench	13 T at 4.2 ^oK
Coil dimensions	25 mm × 70 mm
Total number of racetrack coils in whole magnet	6
Total number of blocks per quadrant in aperture	2 (+1 outside the aperture)
Yoke outer radius	500 mm (same as in D20)
Field harmonics	a few parts in 10^{-5} at 10 mm
Midplane gap (midplane to coil)	5 mm (coil to coil 10 mm)
Minimum coil height in the end	45 mm (Note: coils are not lifted up.)

Case 2: Newer conductor and graded

Central field at quench	14.7 T at 4.2 ^oK
Grading	70 mm divided in two 35 mm layers
Overall current densities	370 A/mm^2 and 600 A/mm^2
Peak fields	16 T and 12.5 T
Copper current density	1500 A/mm^2
Other features are the same as in *case 1*	

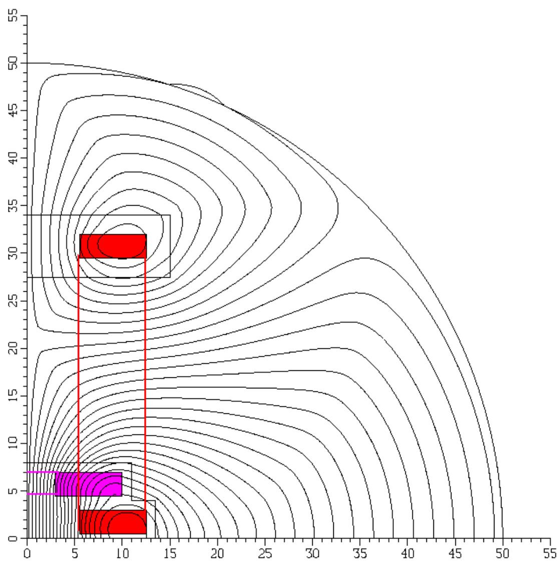

FIG. 12. Cross section of Alternative High Field (≈ 15 T) Race Track Coil Dipole Magnet magnet with Nb_3Sn conductor.

2. Alternative Cos Theta Nb_3Sn dipole

In this case the problem with the brittle and sensitive conductor is solved by winding the coil inside many separate slots cut in metal support cylinders. There is no build up of forces on the coil at the mid-plane. The slots continue round the ends, and thus solve the support problem there too.

Figure 13 shows this alternative Nb_3Sn dipole cos theta design. It is an extension of the concept used to build helical magnets [23] for the polarized proton program at RHIC [24]. The magnet is wound with pre-reacted, kapton-insulated, B-stage impregnated, low current cable. The build up forces is controlled by laying the cables in machined

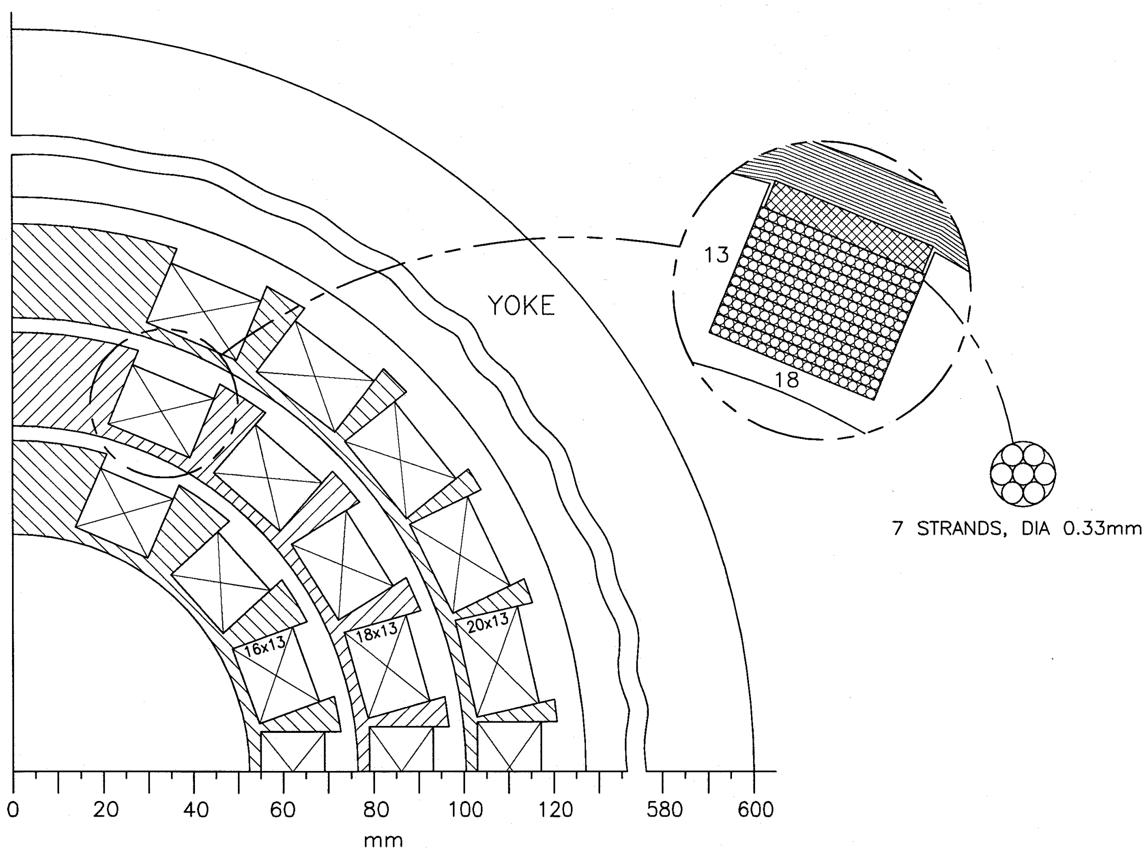

FIG. 13. Cross section of Alternative High Field Slot Dipole made with Nb_3Sn conductor.

slots in a metal support cylinder. After winding, the openings of the slots are bridged by metal spacers and the coils pre compressed inward by winding B-stage impregnated high tensile thread around the spacers. After curing, the outside of each coil assembly is machined prior to its insertion into an outer coil, or into the yoke. There are 3 layers. The inner bore is 55 mm radius, the outer coil radius approximately 118 mm, the yoke inside radius 127 mm rad. The maximum copper current density is 1300 A/mm^2.

Using the same material specification as used in the above high field option, a central short sample field of 13.2 T was calculated. This is somewhat less than the block design discussed above, but could be improved by increasing the cable diameters to improve the currently rather poor (64%) cable to cable-plus-insulator ratio.

3. Study of C-magnet dipole

Figure 14 shows the cross section of a high field dipole magnet in which it was hoped to bring the coils in closer to the beam pipe without suffering excessive heating from beam decay. The coil design [25] appeared reasonable, but the required avoidance of coil heating was not achieved.

Decay electrons are generated at very small angles ($\approx\ 1/\gamma$)to the beam, with energies always lower than that of the beam, and with an average energy about 1/3 of the beam. Such electrons initially spiral inward (to the right in Fig. 14) bent by the high dipole field. In the high energy case, they also radiate a significant fraction of their energy as ($\approx$ 1 GeV) synchrotron gamma rays, some of which finish u p on the outside (to the left in Fig. 14). The concept was to use a very wide beam pipe, allow the electrons to exit between the coils, and be absorbed in an external cooled dump. Unfortunately a preliminary study found that a substantial fraction of the electrons did not reach the dump. They were bent back outward, before reaching it, by the return field of the magnet coils and the nature of the curved ring geometry. Such electrons were then trapped about the null in the vertical field and eventually hit the upper or lower face of the unshielded vacuum pipe. They showered, and deposited unacceptable levels of heat in the coils.

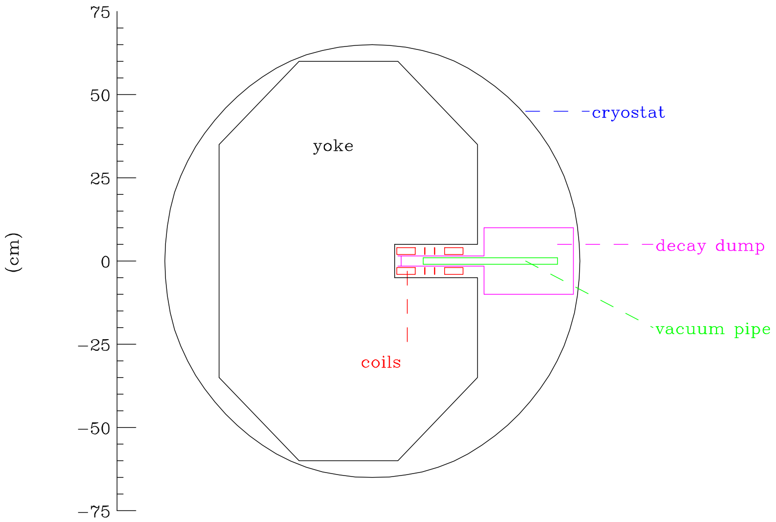

FIG. 14. Cross section of unsuccessful alternative high field C magnet with open mid-plane.

Another idea called for collimators between each bending magnet that would catch such trapped electrons. This option was not studied in detail, but the impedance consequences of such periodic collimators was expected to be unacceptable.

Further study of such options might find a solution, but the use of a thick cylindrical heavy metal shield appears practical, adequate, and is thus the current baseline choice.

H. Energy Scale calibration

In order to scan the width of a Higgs boson of mass around 100 GeV, one needs to measure the energy of the individual muon stores to an accuracy of a few parts per million, since the width of a Higgs boson of that mass is expected to be a few MeV. Assuming that muon bunches can be produced with modest polarizations of ≈ 0.25, and that the polarization can be maintained from turn to turn in the collider, it is possible to use the precession of the polarization in the ring to measure accurately the average energy of the muons [26]. The total energy of electrons produced by muon decay observed in a calorimeter placed in the ring varies from turn to turn due to the $g-2$ precession of the muon spin that is proportional to the Lorentz factor γ of the muon beam. Figure 15 shows the result of a fit of the total electron energy observed in a calorimeter to a functional form that includes muon decay and spin precession [26]. Figure 16 shows the fractional error $\delta\gamma/\gamma$ obtained from a series of such fits plotted against the fractional error of measurement in the total electron energy that depends on the electron statistics. It has been shown [26] that precisions of a few parts per million in γ are possible with modest electron statistics of $\approx 100,000$ detected. It should be noted that there are 3.2×10^6 decays per meter for a muon intensity of 10^{12} muons. In order to maintain the precession of the polarization in a horizontal plane, it is necessary to compensate for the rotation in polarization introduced by the detector solenoid with opposing solenoids placed on either side of the interaction region.

1. Possible Implementation Strategy

Our current plans to measure the energy due to decay electrons entail an electromagnetic calorimeter that is segmented both longitudinally and transversally placed inside an enlarged beam pipe in one of the straight sections in the collider ring. The length of the straight section upstream of the calorimeter can be chosen to control the number of decays (3.2×10^6 decays per meter for a beam intensity of 10^{12} muons) and hence the rate of energy deposition. The sensitive material can be gaseous, since the energy resolution is controlled by decay fluctuations rather than sampling error. In order to measure the total number of electrons entering the calorimeter, we plan to include a calorimeter layer with little absorber upstream of it as the first layer.

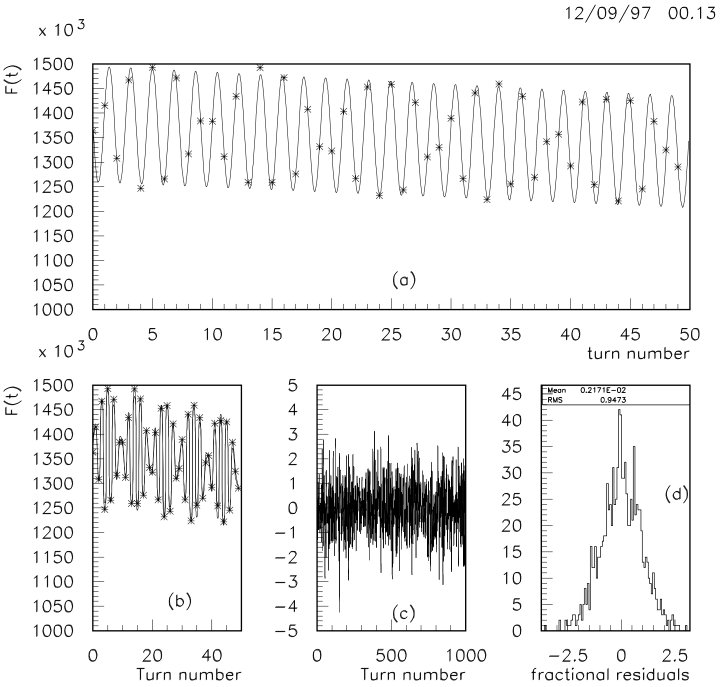

FIG. 15. (a)Energy detected in the calorimeter during the first 50 turns in a 50 GeV muon storage ring (points). An average value of $\hat{P}$=-0.26 is assumed and a fractional fluctuation of 0.5E-2 per point. The curve is the result of a MINUIT fit to the expected functional form. (b) The same fit, with the function being plotted only at integer turn values. A beat is evident. (c) Pulls as a function of turn number (d)Histogram of pulls. A pull is defined by (measured value-fitted value)/(error in measured-fitted).

[1] K. L. Brown and J. Spencer, presented at the Particle Accelerator Conf., Washington. SLAC-PUB-2678 (unpublished).
[2] K.L. Brown, SLAC-PUB-4811; Proc. Capri Workshop, 1988.
[3] K. L. Brown J.J. Murray and T.H. Fieguth, Particle Accelerator Conf., Washington, 1987.
[4] Olivier Napoly, CLIC Final Focus System: Upgraded Version with Increased Bandwidth and Error Analysis, CERN Report CLIC Note 227, 1994.
[5] A. Chao, *Physics of Collective Beam Instabilities in High Energy Accelerators* (John Wiley & Sons, Inc., New York, 1993).
[6] A. Garren and C. Johnstone, Lattice Design for a 100 GeV Muon Collider, presentation at the 4^{th} Int. Conference on Physics Potential and Development of $\mu - \mu$ Colliders, San Francisco, CA, 1997, (unpublished).
[7] C. J. Johnstone and N. V. Mokhov, *Optimization of a Muon Collider Interaction Region with Respect to Detector Backgrounds and the Heat Load to the Cryogenic Systems* , Proceedings of the 1996 DPF/DPB Summer Study on New Directions for High Energy Physics (Snowmass'96) and Fermilab-Conf-96/366, 1996., 1996.
[8] N. Mokhov et al., Scraping Beam Halo in $\mu^+\mu^-$ Colliders, *4th International Conference on Physics Potential and Development of Muon Colliders*, 1997, to be published.
[9] M. Donald et al., Localized Chromaticity Correction of Low-Beta Insertions in Storage Rings, Proc. 1993 Part. Accel. Conf., Washington, D.C., pp. 131, 1993.
[10] W. Wan and C. Johnstone, *Tracking simulations of local, interleaved and noninterleaved chromatic correction sextupoles*, presentation at the Mini-Workshop on Lattice, BNL, 1997, unpublished.
[11] K.-Y. Ng S.Y. Lee and D. Trbojevic, Technical Report No. FNAL-FN595, FNAL (unpublished).
[12] D. Neuffer and W. Wan, COSY transport for μ cooling, presentation at the Mini-Workshop on Cooling, FNAL, 1997, (unpublished).
[13] K.-Y. Ng S.Y. Lee and D. Trbojevic, Phys. Rev **E48**, (1993).
[14] M. Berz, COSY INFINITY, v. 7. User's Guide and Reference Manual, Michigan State University Report, 1996; also at URL http://www.beamtheory.nscl.msu.edu/cosy/.
[15] L. Schachinger and R. Talman, Part. Accel. **22**, 35 (1987).
[16] G. W. Foster and N. V. Mokhov, in *Physics Potential & Development of $\mu^+\mu^-$ Colliders 2^{nd} Workshop* (AIP Press, Woodbury, New York, YEAR).
[17] M. Furman, The Classical Beam-Beam Interaction for the Muon Collider: A First Look, BF-19/CBP-Note-169/LBL-38563,

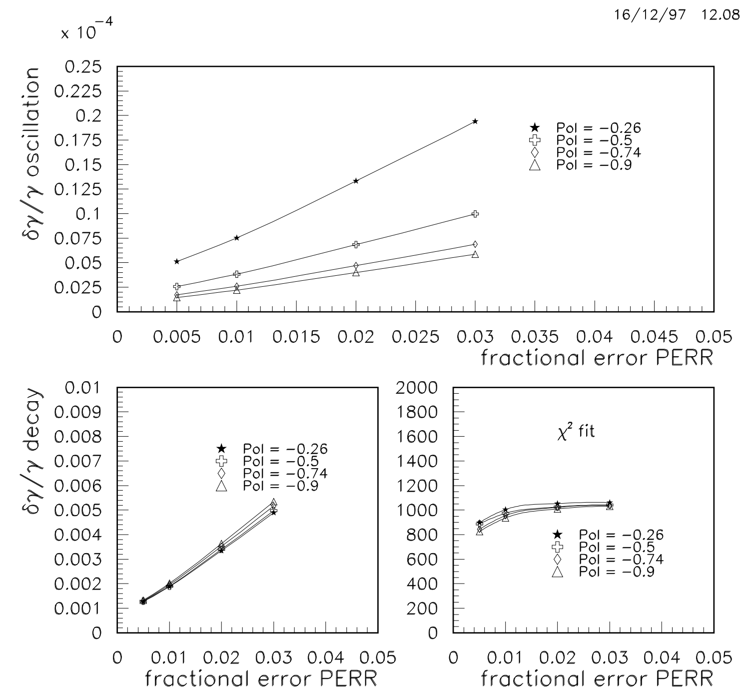

FIG. 16. (a)Fractional error in $\delta\gamma/\gamma$ obtained from the oscillations as a function of polarization $\hat{P}$ and the fractional error in the measurements PERR (b) Fractional error in $\delta\gamma/\gamma$ obtained from the decay term as a function of polarization $\hat{P}$ and the fractional error in the measurements PERR (c) The total χ^2 of the fits for 1000 degrees of freedom. PERR is the percentage measurement error on the total electron energy in the calorimeter measuring the decay electrons.

1996.

[18] P. Chen, in *Proceedings of the Symposium on Physics Potential & Development of $\mu^+\mu^-$ Colliders*, Vol. 51A of *Proceedings Suppl. Nucl Phy B*, edited by D. Cline (North-Holland, The Netherland, 1996), p. 179.

[19] A. M. Sessler W.-H. Cheng and J. Wurtele, in *Proceedings of the 9th Advanced ICFA Beam Dynamics Workshop*, edited by J. C. Gallardo (AIP Press, Woodbury, New York, 1996), Vol. 372.

[20] K.Y. Ng, in *Proceedings of the 9th Advanced ICFA Beam Dynamics Workshop*, edited by J. C. Gallardo (AIP Press, Woodbury, New York, 1996).

[21] Muon Collider Collaboration, in *Proceedings of the 1996 DPF/DPB Summer Study on High-Energy Physics Snowmass'96,* New Directions for High-Energy Physics (Stanford Linear Accelerator Center, Menlo Park, CA, 1997), for updated information, see the Muon Collider Collaboration WEB page at the URL, http://www.cap.bnl.gov/mumu/.

[22] N. V. Mokhov and S. I. Striganov, *Proceedings of the 9th Advanced ICFA Beam Dynamics Workshop* (AIP Press, Woodbury, New York, 1996), Vol. 372, pp. 234–256; also Fermilab–Conf–96/011 (1996).

[23] E. Willen et al., A Helical Magnet Design for RHIC, *Proceedings 1997 Particle Accelerator Conference*, Vancouver, BC, Canada, 1997.

[24] T. Roser (Spokesperson) et al., Conceptual Design for the Acceleration of Polarized Protons in RHIC, available at the URL http://www.ags.bnl.gov/ roser/cdr07034/cdr07034.html, 1995.

[25] R. Willen, (private communication).

[26] Rajendran Raja and Alvin Tollestrup, Calibrating the energy of a 50 × 50 GeV Muon Collider using $g-2$ spin precession, Fermilab-PUB-97-402; submitted to Phys. Rev. D, hep-ex/9801004, 1998.